

HIGH-HARMONIC PLASMA EMISSION INDUCED BY ELECTRON BEAMS IN WEAKLY MAGNETIZED PLASMAS

CHUANYANG LI (李传洋),^{1,2} YAO CHEN (陈耀),^{1,3} ZILONG ZHANG (张子龙),³ HAO NING (宁昊),¹ AND TANGMU LI (李汤姆)¹

¹*Institute of Frontier and Interdisciplinary Science, Shandong University, Qingdao, Shandong, 266237, People's Republic of China*

²*College of Physics and Electronic information, Dezhou University, Dezhou, Shandong, 253023, People's Republic of China*

³*Institute of Space Sciences, Shandong University, Shandong, 264209, People's Republic of China*

(Received ***; Revised ***; Accepted ***)

ABSTRACT

Electromagnetic radiation at higher harmonics of the plasma frequency ($\omega \sim n\omega_{pe}, n > 2$) has been occasionally observed in type II and type III solar radio bursts, yet the underlying mechanism remains undetermined. Here we present two-dimensional fully kinetic electromagnetic particle-in-cell simulations with high spectral resolution to investigate the beam-driven plasma emission process in weakly magnetized plasmas of typical coronal conditions. We focused on the generation mechanisms of high-harmonic emission. We found that a larger beam velocity (u_d) favors the generation of the higher-harmonic emission. The emissions grow later for higher harmonics and decrease in intensity by ~ 2 orders of magnitude for each jump of the harmonic number. The second and third harmonic (H_2 and H_3) emissions get closer in intensity with larger u_d . We also show that (1) the H_3 emission is mainly generated via the coalescence of the H_2 emission with the Langmuir waves, i.e., $H_2 + L \rightarrow H_3$, wherein the coalescence with the forward-propagating beam-Langmuir wave leads to the forward-propagating H_3 , and coalescence with the backward-propagating Langmuir wave leads to the backward-propagating H_3 ; and (2) the H_4 emission mainly arises from the coalescence of the H_3 emission with the forward- (backward-) propagating Langmuir wave, in terms of $H_3 + L \rightarrow H_4$.

Keywords: Plasma astrophysics (1261); Solar electromagnetic emission(1490); Solar radio emission(1522); Radio bursts (1339); Space plasmas(1544); Solar coronal radio emission (1993);

1. INTRODUCTION

Plasma emission (PE) is defined as electromagnetic (EM) radiation at frequencies close to the plasma frequency ω_{pe} (F) and its second harmonic (H_2). Several types of solar radio burst, the radio radiation from the outer heliospheric boundary, and some radio emissions from the planetary magnetosphere have been understood as PE (e.g., Etcheto & Faucheux 1984; Cairns 1995, 1998; Gurnett et al. 1998; Cairns & Zank 2002; Kuncic & Cairns 2005; Chen et al. 2014; Vasanth et al. 2016, 2019; Lv et al. 2017; Li et al. 2017; Piša et al. 2017; Tasnim et al. 2022). Emission, probably at the third harmonic (H_3), has been occasionally reported for type II (Bakunin et al. 1990; Kliem et al. 1992; Zlotnik et al. 1998; Brazhenko et al. 2012) and type III solar radio bursts (Kundu 1965; Takakura & Yousef 1974; Zlotnik 1978; Cairns 1986; Reiner et al. 1992; Reiner & MacDowall 2019). For other examples, Cairns (1986) reported harmonics at $n\omega_{pe}$ ($n = 3-5$) in the foreshock region of the bow shock with the ISEE1 data, while Reiner & MacDowall (2019) detected possible H_3 emissions in interplanetary type III bursts based on the Wind data.

Ginzburg & Zheleznyakov (1958) proposed the original framework of the theory of PE, which has been developed into the standard PE model (e.g., Melrose 1970a,b; Zheleznyakov & Zaitsev 1970a,b; Melrose 1980, 1987; Cairns 1987; Robinson et al. 1994). The model involves a multistep nonlinear process of wave-particle and wave-wave interactions: (1) efficient excitation of Langmuir (L) turbulence by electron beams through the kinetic bump-on-tail instability, (2) scattering of L waves by ion-acoustic (IA) waves or ion density inhomogeneities to generate the fundamental emission and/or backward-propagating Langmuir (L') waves ($L \pm IA \rightarrow F$ and $L \pm IA \rightarrow L'$), and (3) resonant coupling of forward- and backward-propagating Langmuir turbulence to generate the harmonic emission ($L + L' \rightarrow H_2$). The standard PE theory has been widely used to explain radio bursts in space and astrophysical plasmas, such as solar radio bursts in terms of types I–V (see, e.g., Chen et al. 2014; Vasanth et al. 2016; Lv et al. 2017; Li et al. 2017; Vasanth et al. 2019). Numerical verifications based on fully kinetic EM particle-in-cell (PIC) simulations (e.g., Thurgood & Tsiklauri 2015; Che et al. 2017; Henri et al. 2019; Ni et al. 2020; Chen et al. 2022; Zhang et al. 2022) or weak turbulence theory have been performed (e.g., Yoon 2000, 2005, 2006; Yoon et al. 2012; Ziebell et al. 2015, 2016; Lee et al. 2019, 2022).

However, the generation mechanism of high-harmonic emissions (H_3, H_4, \dots) remains inconclusive (Zheleznyakov & Zlotnik 1974; Cairns 1987; Yin et al. 1998; Zlotnik et al. 1998; Ziebell et al. 2015). Three different mechanisms have been proposed: (1) coalescence of three L waves in terms of $L + L' + L'' \rightarrow H_3$ (Kliem et al. 1992); (2) coalescence of an L wave with H_2 in terms of $L + H_2 \rightarrow H_3$ (Zlotnik 1978), where this mechanism has been generalized by Cairns (1988) as $L + H_n \rightarrow H_{n+1}$; and (3) $L + L_n \rightarrow H_{n+1}$ (Yi et al. 2007), i.e., coalescence of the primary L wave with the n th-harmonic L mode (L_n).

Earlier numerical studies mainly focused on the generation of the F and H_2 emissions (e.g., Pritchett & Dawson 1983; Yin et al. 1998; Kasaba et al. 2001), with few reports on high-harmonic emission. Using the two-dimensional relativistic EM PIC code to simulate the beam-plasma interaction process (Matsumoto & Omura 1993), Rhee et al. (2009) found that high-harmonic emission (up to the fifth) can be generated with the beam velocity exceeding $0.5c$. By examining the radiation patterns and the temporal correlation between the electrostatic (ES) and EM waves, they suggested that the H_3 (H_4) emission resulted from the merging of the H_2 (H_3) emission with the L waves, in agreement with the second process mentioned above. Note that Rhee et al. (2009) utilized a relatively small domain ($512 \lambda_{De} \times 512 \lambda_{De}$, where λ_{De} is the electron Debye length) and a limited duration ($328 \omega_{pe}^{-1}$) with a relatively low number of macroparticles (the number of macroparticles per cell per species, NPPCPS, which, for background electrons and protons and beam electrons, was 80, 80, and 8, respectively). These limitations led to excessive numerical noise along dispersion curves and a limited resolution. Thus, further validation is required.

Recently, Krafft & Savoini (2022) conducted two-dimensional PIC simulations in weakly magnetized plasmas using larger-domain ($1448 \lambda_{De} \times 1448 \lambda_{De}$), longer-duration ($9000 \omega_{pe}^{-1}$), and larger NPPCPS

values (1800, 1800, 1800). Their study focused on the coalescence processes to generate H_3 and H_4 in the beam-plasma system with or without density fluctuations. They suggested the following processes for H_3 : $H_2 + L'(L'') \rightarrow H_3$, where $L'(L'')$ is supposed to be the product of the first (second) cascade of the ES decay of the beam-Langmuir (BL) waves ($L \rightarrow L' + S'$ and $L' \rightarrow L'' + S''$); a very similar process has been suggested for H_4 . They did not reject the possibility of other processes such as $L'_2 + L \rightarrow H_3$ and $L'_3 + L \rightarrow H_4$.

With careful evaluations, we suggest that the result of [Krafft & Savoini \(2022\)](#) remains questionable and should be further tested due to the following concerns.

(1) Regarding the Fourier analysis used to obtain the high-harmonic spectra in the wavevector space, the authors restricted the frequency range to a small window centered around $\omega_n \approx n\omega_{pe}$ (refer to their Figures 1(c) and (d) and 5(c) and (d)). This means only signals within the prescribed narrow range have been processed. Such analysis could not tell the existence of high-harmonic radiation since, even in the thermal case, such analysis can give enhanced signals around ω_n , or any frequency ($> \omega_{pe}$). This is due to the local enhancement of numerical noise along dispersion curves with PIC simulations. We have confirmed this with our result, following the same procedure as employed by [Krafft & Savoini \(2022\)](#).

(2) Regarding the uncertainties of the energy evaluation of H_4 , the H_4 intensity is only marginally larger than the initial value in their homogeneous case, with no discernable increase of H_4 intensity in the other case with density fluctuations (see Figures 2(a) and 4(a) in [Krafft & Savoini 2022](#)). This raises doubts as to whether the obtained H_4 emission is really excited by the beam-plasma interaction or is simply a part of the numerical noise.

Another point is that the H_3 and H_4 emissions can be excited at a beam velocity of $0.25c$ according to [Krafft & Savoini \(2022\)](#). This contradicts the abovementioned result of [Rhee et al. \(2009\)](#). To clarify these issues, we repeated the simulations of the beam interaction with a uniform plasma, with basically the same configurations as used by [Krafft & Savoini \(2022\)](#), such as the simulation domain, grid spacing, number of particles, etc.. This is done with the Vector-PIC (VPIC) code (described in the next section) and the same computational time ($9000 \omega_{pe}^{-1}$). Our simulations only yielded weak H_2 emission, without significant high-harmonic emissions whose generation mechanism thus remains to be revealed. This presents the main purpose of the present study.

2. NUMERICAL SETUP AND PARAMETERS

The simulations are performed using the VPIC code developed and released by Los Alamos National Labs, which is two-dimensional in space and three-dimensional for particle velocity and EM fields. VPIC employs a second-order, explicit, leapfrog algorithm to update charged particle positions and velocities in order to solve the relativistic kinetic equation for each species, along with a full Maxwell description for electric and magnetic fields evolved via a second-order finite-difference time-domain solver ([Bowers et al. 2008a,b, 2009](#)). Periodic boundary conditions are used. The background magnetic field is set to be $\vec{B}_0 (= B_0 \hat{e}_z)$, and the wavevector \vec{k} is in the xOz plane. The plasmas consist of three components, including background electrons and protons with a Maxwellian distribution and an electron beam with the following velocity distribution function:

$$f_e = A_e \exp\left(-\frac{u_{\perp}^2}{2u_0^2} - \frac{(u_{\parallel} - u_d)^2}{2u_0^2}\right) \quad (1)$$

where u_{\parallel} and u_{\perp} are the parallel and perpendicular components of the momentum per mass, u_d is the average drift momentum per mass of the beam electrons, u_0 is the thermal velocity of energetic electrons, and A_e is the normalization factor.

Based on the observations of solar radio bursts (e.g., [Wild & McCready 1950](#); [Wild et al. 1959](#); [Alvarez & Haddock 1973](#); [Reid et al. 2014](#)) and in situ data of energetic electrons (e.g., [Lin et al. 1973](#),

1981, 1986), the drift speed of the electron beam is set to be $u_d = 0.3\text{--}0.7c$ and the thermal velocity of background and beam electrons with a fixed value of $u_0 = 0.028c$. The ratio of plasma oscillation frequency to electron gyrofrequency (ω_{pe}/Ω_{ce}) is set to be 100. The density ratio of beam-background electrons (n_b/n_0) is set to be 0.5%. All particles initially distribute homogeneously in space.

To facilitate the comparison with Krafft & Savoini (2022), we use the same numerical configurations, such as the simulation domain ($L_x = L_z = 1024 \Delta$, where $\Delta = \sqrt{2} \lambda_{De}$ is the grid spacing and λ_{De} is the Debye length of the background electrons), the unit of time (ω_{pe}^{-1}), the simulation time $3000 \omega_{pe}^{-1}$ and the time step $\Delta t = 0.01 \omega_{pe}^{-1}$. The corresponding resolvable range of $|k|$ is $[0.15, 79] \omega_{pe}/c$, and the range of ω is $[0.002, 6.4] \omega_{pe}$ (for the time interval of $3000 \omega_{pe}^{-1}$). The NPPCPS is 1800 for background electrons and 900 for both background protons and beam electrons. The ratio of the ion to the electron plasma temperatures is set to be $T_i/T_e = 0.1$ to avoid strong Landau damping. At the start of the simulation, we maintain charge neutrality by setting proper weights to each species of macroparticle and neutralize the electron beam current by setting a proper bulk speed to the background electrons (see, e.g., Henri et al. 2019; Chen et al. 2022; Zhang et al. 2022).

3. NUMERICAL RESULTS

We first present the reference case (Case R) with beam velocity $u_d = 0.5c$ and the realistic proton-electron mass ratio ($m_i/m_e = 1836$) that will be compared with the corresponding thermal case (Case T) to tell the excitations of waves. Then, we vary u_d to investigate its effect. One experiment with a larger mass ratio ($m_i/m_e = 18360$) is conducted to expand the investigation.

3.1. Wave Analysis for Case R

We first present the energy curves of the six field components and the negative change of the total kinetic energy of all electrons ($-\Delta E_k$) for Cases R and T (Figure 1(a) and (b)). The energies of all field components in Case R are significantly stronger than those in Case T by at least 2–4 orders of magnitude. This means these fields arise due to the beam-plasma interaction. Based on the energy profiles, the initial stage (0–100 ω_{pe}^{-1}) is characterized by the rapid rise of E_x and E_z in energy, corresponding to the growth of the primary BL mode. At the end of this stage, $-\Delta E_k$ reaches $\sim 4\%$ of E_{k0} . The maximum of $-\Delta E_k$ is $\sim 6\%$ of E_{k0} , obtained at $\sim 300 \omega_{pe}^{-1}$. From 100 to 900 ω_{pe}^{-1} , the BL mode saturates at an energy level of $0.03 E_{k0}$. This is followed by the damping stage, within which the wave energy is returned to electrons. Between 0 and 2000 ω_{pe}^{-1} , the intensities of the other three components (E_y , B_x , and B_z) slowly rise and saturate. The E_y component is mainly associated with the Z mode and the harmonic radiation, and the B_x and B_z components mainly carry the W mode, as well as the harmonic radiation.

Figure 2 presents wave-energy maps in the wavevector (\vec{k}) space for the ES modes around ω_{pe} , $2 \omega_{pe}$, and $3 \omega_{pe}$ and the harmonic radiations. The maps present the intensity maxima of waves at the corresponding \vec{k} , regardless of their frequencies. The mode nature can be identified with the analytic dispersion curves plotted in Figure 3 (and the accompanying movies). The modes excited here include the L_3 mode, the L_2 and L_{2b} modes, the BL and L_b modes, and the H_2 and H_3 emissions. Here, the subscript ‘‘f’’ (‘‘b’’) denotes the forward (backward)-propagating portion of the corresponding mode, while the number in the subscript indicates the harmonics. The dominant E_x and E_z components correspond to the primary forward-propagating ES-BL mode (Figure 2(c)). The BL mode extends $\sim \pm 77^\circ$ away from the parallel direction in E_z , with a significant perpendicular electric field component of E_x . The movie accompanying Figure 2 shows its evolution in the \vec{k} space. During the rapid-excitation stage, the E_z component presents a rather narrow range in the \vec{k} space, with $1.5 \leq k_{\parallel}(\omega_{pe}/c) \leq 3.5$ and $k_{\perp}(\omega_{pe}/c) \leq 8$; later, it expands toward larger k_{\parallel} . It is within the range of $2 \leq k_{\parallel}(\omega_{pe}/c) \leq 15$ at $\sim 900 \omega_{pe}^{-1}$, followed by the decline of intensity and the shrinkage of the \vec{k} range.

Figures 2(c) and 3(c) reveal the presence of two additional L components on the left (backward) side of the BL mode, referred to as the forward- and backward-propagating generalized Langmuir (GL) modes, repre-

sented by GL_f and L_b , respectively (see also [Chen et al. 2022](#); [Zhang et al. 2022](#)). As depicted in Figure 2 and its accompanying movie, both the GL_f and L_b modes experience delayed growth with weaker intensities compared to the BL mode. The k_{\parallel} range of the GL_f mode remains relatively narrow ($0 \leq k_{\parallel}(\omega_{pe}/c) \leq 2$), while the k_{\parallel} of the L_b mode expands gradually and reaches $k_{\parallel}(\omega_{pe}/c) \sim -15$ at $\sim 900 \omega_{pe}^{-1}$, with an angular pattern resembling that of the primary BL mode. Subsequently, both modes damp with decreasing ranges of \vec{k} .

The intensities of the BL, L_2 , and L_3 modes decrease gradually with increasing ranges of k_{\parallel} . The k_{\parallel} range of L_2 expands from $[3, 6] \omega_{pe}/c$ initially to $[5, 15] \omega_{pe}/c$ around $900 \omega_{pe}^{-1}$. For L_3 , its k_{\parallel} range extends from $[6, 8]$ to $[9, 13] \omega_{pe}/c$ during $[100, 900] \omega_{pe}^{-1}$. The L_{2b} mode appears around $650 \omega_{pe}^{-1}$, within $-10 \leq k_{\parallel}(\omega_{pe}/c) \leq -4$. After $\sim 900 \omega_{pe}^{-1}$, these ES waves begin to decay with the shrinkage of the k_{\parallel} range.

The circular patterns shown in Figure 2(d) represent the H_2 and H_3 radiation. We observe no signatures of higher-harmonic emissions. According to the movie accompanying Figure 2, the H_3 emission grows after H_2 . The H_2 radiation is stronger than H_3 , and the forward-propagating portion of H_3 is stronger than the backward-propagating portion.

In Figure 3, we present the $\omega - k$ dispersion analysis along the propagation angle $\theta_{kB} = 30^\circ$. The accompanying movie shows the variation of the dispersion relation at a step of 10° . Note that the frequency ranges of H_2 and H_3 vary similarly with θ_{kB} . The overplotted dashed lines represent the dispersion relations of the L wave with thermal effects ($\omega^2 = \omega_{pe}^2(1 + 3k^2\lambda_{De}^2)$) and wave modes given by the classical cold plasma magnetoionic theory. Table 1 summarizes the ω and k ranges for each mode just before the rapid decay of the ES modes ($\sim 900 \omega_{pe}^{-1}$).

We examine the temporal development of various wave modes with energy profiles for specific field component(s) (see Figures 1(c) and (e)), which are calculated by integrating the field energy within a specified spectral range (Figure 3(c)) along the corresponding dispersion curve according to Parseval's theorem. The forward-propagating BL, L_2 , and L_3 modes display the strongest and fastest growth; their intensities saturate around $100 \omega_{pe}^{-1}$, then remain at an almost constant level before declining gradually after $\sim 900 \omega_{pe}^{-1}$. The L_b mode is slightly stronger than GL_f , both with similar energy profiles. Both modes grow gradually over time, reaching the maximum level near $900 \omega_{pe}^{-1}$. The L_{2b} mode shows a delayed onset of growth at $\sim 600 \omega_{pe}^{-1}$, followed by further enhancement and subsequent decay to the thermal noise level.

The comparison with the corresponding thermal case (Figures 1(e) and (f)) confirms the significant enhancement of the H_2 and H_3 emissions over thermal noise, while emissions at the fourth and higher harmonics are absent.

The energy profiles of H_2 and H_3 are similar. Both modes get enhanced gradually over time, reaching the saturation level near $900 \omega_{pe}^{-1}$ and remaining at a nearly constant level thereafter. However, the onset of H_3 is later by $\sim 400 \omega_{pe}^{-1}$ compared to H_2 . The H_3 intensity gets weaker than H_2 , and their intensity ratio (W_{H_2}/W_{H_3}) at saturation is ~ 120 .

The forward- (f) and backward- (b) propagating portions of H_2 show little difference, and the intensity ratio ($W_{H_{2f}}/W_{H_{2b}}$) at saturation is ~ 1.4 . However, the forward-propagating portion of H_3 is much stronger than its backward-propagating portion, with $W_{H_{3f}}/W_{H_{3b}} \sim 4$ at saturation, agreeing with the wave-energy maps shown in Figure 2(d).

3.2. Effect of the Beam Velocity and the Mass Ratio (m_i/m_e)

Two sets of numerical experiments are carried out. We first investigate the effect of the beam velocity (u_d) with the physical mass ratio ($m_i/m_e = 1836$). This gives four additional cases (A, B, C, and D), corresponding to $u_d = 0.3c, 0.4c, 0.6c,$ and $0.7c$, respectively. We then investigate the effect of m_i/m_e , since this parameter can affect the intensity of the ES modes and the radiation process ([Chen et al. 2022](#); [Zhang et al. 2022](#)). This gives Case E with $u_d = 0.5c$ and $m_i/m_e = 18360$.

Figures 4 and 5 present the wave-energy maps in the \vec{k} space for Cases A ($u_d = 0.3c$) and D ($u_d = 0.7c$), respectively. The accompanying movies show the evolution. In comparison with Case R ($u_d = 0.5c$), the forward-propagating ES modes (BL, L_2 and L_3) have larger k_{\parallel} values in Case A, but smaller values in Case D. For instance, the k_{\parallel} range of BL in Case A extends from $[3, 6.5] \omega_{pe}/c$ initially to $[4, 11] \omega_{pe}/c$, while it expands from $[1, 2] \omega_{pe}/c$ to $[1.5, 15] \omega_{pe}/c$ in Case D.

For EM harmonics, the H_2 and H_3 emissions exhibit weaker intensities in Case A than in Case R, with H_3 only presenting a faint backward-propagating part (H_{3b} ; see Figure 4(d) and the accompanying movie). Figure 5(d) shows the significant enhancements of H_2 and H_3 , with the additional appearance of H_4 emission in the forward-propagation direction (H_{4f}). According to the movie accompanying Figure 5, the H_3 emission grows after H_2 , and H_4 grows after H_3 .

Figure 6 illustrates the temporal energy profiles of the ES modes for different cases. As u_d increases from $0.3c$ to $0.7c$, the intensity maximum of each ES mode increases correspondingly. Among them, the BL, L_2 , and L_3 modes exhibit a similar trend, with the onset of the decay being earlier for larger u_d . The L_b and GL_f modes arise simultaneously and both grow and decay faster with increasing u_d . Both modes reach their intensity maximum earlier with increasing u_d . The times of their intensity maxima are indicated by circles in Figure 6 at 3000, 1282, 933, 735, and 677 ω_{pe}^{-1} for L_b mode and 1622, 1294, 993, 848, and 766 ω_{pe}^{-1} for GL_f mode. These times correspond to the start of the decay of the respective BL mode.

Figure 7 illustrates the energy profiles of H_2 and H_3 . Both show considerable enhancements in Cases B–E and R, while significant H_4 emission appears only in Cases C and D, corresponding to $u_d = 0.6c$ and $0.7c$. For different cases, the energy profiles of H_2 , H_3 , and H_4 are quite similar, with comparable growth rates and saturation times. The H_2/H_3 emissions saturate earlier with increasing u_d . The H_2 exhibits higher intensity and grows earlier than H_3 . The H_2/H_3 energy ratio (W_{H_2}/W_{H_3}) decreases with increasing u_d . For instance, as u_d increases from $0.3c$ to $0.7c$, W_{H_2}/W_{H_3} decreases from 206.8 to 44.1; see Table 2 for details. Likewise, H_3 exhibits higher intensity and grows earlier than H_4 . In Cases C and D, the H_3/H_4 energy ratios (W_{H_3}/W_{H_4}) are 93.6 and 88.5, respectively.

The H_{2f} portion is stronger than H_{2b} for smaller u_d ($= 0.3c$ and $0.4c$), while H_{2f} is closer to H_{2b} in intensity with larger u_d (from $0.5c$ to $0.7c$). Regarding H_3 , the H_{3b} portion is stronger than H_{3f} with $u_d = 0.3c$ (Case A). As u_d increases to $0.4c$ (Case B), H_{3b} is initially weaker, yet it gets stronger than H_{3f} later. For $u_d \geq 0.5c$, H_{3f} is always stronger than H_{3b} . In Cases C and D, H_{4f} is always stronger than H_{4b} .

3.3. On the Generation Mechanism of H_3

As introduced, three nonlinear wave-wave coupling processes have been proposed to account for the H_3 emission. The modes involved must satisfy the matching conditions: $\vec{k}_1 + \vec{k}_2 = \vec{k}_3$ and $\omega_1 + \omega_2 = \omega_3$. For Case R with $u_d = 0.5c$, according to the ω and k ranges of various modes listed in Table 1, three processes can satisfy the matching conditions: (a) $BL + L_{2b} \rightarrow H_3$, (b) $L_b + L_2 \rightarrow H_3$, and (c) $BL/L_b + H_2 \rightarrow H_3$.

These possibilities can be further evaluated by analyzing the energy profiles of relevant modes. From Figures 1(c) and (e), we have (1) the energy curves of L_b , H_2 , and H_3 are correlated with similar growth rates and consistent saturation times ($\sim 900 \omega_{pe}^{-1}$); (2) H_2 exhibits higher intensity and grows earlier than H_3 ; (3) L_{2b} is much weaker than other modes and damps to the noise level shortly after the brief enhancement; and (4) H_3 grows earlier than L_{2b} .

The first point suggests that L_b may play a role in the generation of both H_2 and H_3 . Combining the first two points, H_2 may get involved in generating H_3 , which supports process (c).

The third and fourth points rule out the participation of L_{2b} in generating H_3 , i.e., process (a).

Process (b) ($L_b + L_2 \rightarrow H_3$) can be largely rejected by considering the late-stage (say, after $t = 2000 \omega_{pe}^{-1}$) characteristics of H_3 and L_2 in Cases A, B, and E. We observe from Figures 7(a), (b), and (f) that H_3 presents persistent enhancement during this late stage. Yet, according to Figures 6(a), (b), and (f) and the movies accompanying Figure 4, in the late stage, (1) in Cases A and B, L_2 damps significantly and approaches its

initial level of numerical noise; and (2) in Case A the k_{\parallel} of L_2 shifts from the earlier range of $\sim 11\text{--}17 \omega_{pe}/c$ to $\sim 13\text{--}17 \omega_{pe}/c$, while that of L_b remains in the range of $-6\text{--}0 \omega_{pe}/c$, making it impossible to meet the corresponding matching condition of process (b). A similar shift occurs to Case E in which the k_{\parallel} of L_2 shifts from the earlier range of $\sim 6\text{--}11$ to $\sim 9\text{--}12 \omega_{pe}/c$ while that of L_b remains in the range of $-7\text{--}0 \omega_{pe}/c$, making it difficult to meet the corresponding matching condition for the generation of H_{3b} with process (b). We conclude that these observations do not favor the significance of process (b) in generating H_3 .

Thus, the most likely process to generate H_3 is (c), $BL/L_b + H_2 \rightarrow H_3$. Based on the matching conditions of three-wave interaction, we can further separate the process into two subprocesses: $BL + H_{2b} \rightarrow H_{3f}$ and $L_b + H_{2f} \rightarrow H_{3b}$. Note that H_{3f} is stronger and rises earlier than H_{3b} , indicating that the process $BL + H_{2b} \rightarrow H_{3f}$ is more effective.

We observe a different directional pattern of H_3 in different cases (A, B, and R). This can be used to constrain the generation mechanism of H_{3f} and H_{3b} . According to Figure 4 and the accompanying movie, the k value of the BL mode (k_{BL}) is too large in Case A ($u_d = 0.3c$) to coalesce with H_2 so as to generate H_{3f} ; this explains the absence of H_{3f} in this case. On the other hand, L_b has the appropriate wavenumber to coalesce with H_2 and generate H_{3b} . For Case B with $u_d = 0.4c$ (see the second part of the accompanying movie), the value of k_{BL} allows the occurrence of the process $BL + H_{2b} \rightarrow H_{3f}$. Note that k_{BL} increases with increasing time; this makes it more difficult to meet the corresponding matching conditions, while the conditions for $L_b + H_{2f} \rightarrow H_{3b}$ can still be satisfied. This can explain the relative intensity variation of H_{3b} and H_{3f} . For Case R with $u_d = 0.5c$ (see Figure 2 and the accompanying movie), both the BL and L_b modes can coalesce with H_2 during the simulation. We get a stronger H_{3f} than H_{3b} since BL is always stronger than L_b .

Note that in Case A we observed the simultaneous presence of GL_f and H_2 , yet the H_{3f} radiation is always at the noise level. This indicates that the process of $GL_f + H_2 \rightarrow H_3$ is not important here.

3.4. On the Generation Mechanism of H_4

In the following, we discuss the generation mechanism of H_4 . Based on the matching conditions, the following processes are possible: (a) $BL + L_{3b} \rightarrow H_4$, (b) $L_b + L_3 \rightarrow H_4$, (c) $BL/L_b + H_3 \rightarrow H_4$, and (d) $L_2/L_{2b} + H_2 \rightarrow H_4$.

First, we can exclude process (a) involving the L_{3b} mode. According to Figures 6(d) and (e) and 7(d) and (e), during the initial growth of H_4 L_{3b} is at the noise level before $600 \omega_{pe}^{-1}$ and then presents a local peak from 600 to $800 \omega_{pe}^{-1}$. Therefore, it is unlikely to be important for the radiation of H_4 .

We can also exclude process (b) based on the following two aspects. First, according to Figures 6(d) and (e) and 7(d) and (e), L_b first increases and then decreases in intensity along with the H_4 growth, while L_3 exhibits a decreasing trend in intensity. This is different from the H_4 intensity profile. Second, L_3 does not change much in intensity when u_d increases from $0.6c$ to $0.7c$, while H_4 reveals significant enhancement.

We can further exclude process (d). From Figure 7(e), H_3 starts to grow earlier than H_4 . As stated earlier, H_2 contributes to the H_3 radiation. If it also contributes to the H_4 radiation, e.g., via process (d), then H_3 and H_4 shall rise at a close time. This is inconsistent with our simulation. In addition, when u_d increases from $0.6c$ to $0.7c$, L_{2b} does not change much in intensity, while H_4 presents substantial enhancement (see Figures 7(d) and (e)). This indicates that the process involving L_{2b} in (d) can be ruled out.

Thus, we are left with process (c), with $BL/L_b + H_3 \rightarrow H_4$. This is supported by the similar intensity profiles of L_b , H_3 , and H_4 . If further taking the matching conditions into account, we find that the following subprocesses may act in the system: $BL + H_{3b} \rightarrow H_{4f}$ and $L_b + H_{3f} \rightarrow H_{4b}$.

4. CONCLUSIONS AND DISCUSSION

In this study, we conduct fully EM PIC simulations to investigate the interaction between beam electrons and a weakly magnetized plasma with the solar coronal-interplanetary conditions. The purpose is to reveal

the generation mechanism of high-harmonic plasma radiations. We obtained significant second, third, and fourth harmonic (H_2 , H_3 , and H_4) radiations. The neighboring harmonics are different in intensity by about 2 orders of magnitude, with higher harmonics being weaker. Cases with larger beam velocities tend to favor the generation of higher harmonics and stronger radiation for the specific harmonic, which is consistent with the statement of Rhee et al. (2009), “by increasing the beam velocity, the present case allows for the excitation of higher-harmonic modes.” We suggest that the H_3 radiation is mainly generated via the process of $H_2 + BL/L_b \rightarrow H_3$ and the H_4 radiation is mainly generated via the process of $H_3 + BL/L_b \rightarrow H_4$, with the forward portion given by the coalescence of H_2 (H_3) with BL mode and the backward portion given by its coalescence with L_b .

The obtained results are helpful to understand the data of solar radio bursts with high-harmonic emission. For instance, the presence of H_3 emission in observations suggests that the energetic electron beam has a higher-than-usual velocity (say, $> \sim 0.5c$), and the intensity ratio of H_3 and H_2 depends on the beam velocity, with a larger intensity ratio corresponding to a faster beam.

According to our earlier simulations (Chen et al. 2022; Zhang et al. 2022) that investigated the PE process for weakly magnetized plasmas with $\omega_{pe}/\Omega_{ce} = 10$ and nonmagnetized plasmas (i.e., $\omega_{pe}/\Omega_{ce} \sim \infty$), the excitation of primary modes and escaping emissions is quite similar for these two cases. Thus, we expect that the major conclusions deduced here still hold for other weakly magnetized plasmas as long as the values of ω_{pe}/Ω_{ce} are much larger than unity.

ACKNOWLEDGEMENTS

This study is supported by NNSFC grants (Nos. 12103029, 1973031, 12203031), a NSFSP (Natural Science Foundation of Shandong Province) grant (No. ZR2021QA033) and the China Postdoctoral Science Foundation (No. 2021M691904). The authors acknowledge the National Supercomputer Centers in Tianjin and the Beijing Super Cloud Computing Center (BSCC; <http://www.blsc.cn/>) for providing high-performance computing (HPC) resources, and the open-source Vector-PIC (VPIC) code provided by Los Alamos National Labs (LANL). The authors are grateful to the anonymous referee for valuable comments.

REFERENCES

- Alvarez, H. & Haddock, F. T. 1973, *SoPh*, 30, 175.
doi:10.1007/BF00156186
- Bakunin, L. M., Ledenev, V. G., Kosugi, T., et al. 1990, *SoPh*, 129, 379. doi:10.1007/BF00159048
- Bowers, K. J., Albright, B. J., Yin, L., et al. 2008a, *Physics of Plasmas*, 15, 055703. doi:10.1063/1.2840133
- Bowers, K. J., Albright, B. J., Bergen, B., et al. 2008b, in *SC '08: Proc. 2008ACM/IEEE Conf. on Supercomputing* No. 63 (Piscataway, NJ: IEEE press), 1 doi: 10.1109/SC.2008.5222734.
- Bowers, K. J., Albright, B. J., Yin, L., et al. 2009, *Journal of Physics Conference Series*, 180, 012055.
doi:10.1088/1742-6596/180/1/012055
- Brazhenko, A. I., Melnik, V. N., Konovalenko, A. A., et al. 2012, *Odessa Astronomical Publications*, 25, 181
- Cairns, I. H. 1986, *J. Geophys. Res.*, 91, 2975.
doi:10.1029/JA091iA03p02975
- Cairns, I. H. 1987, *Journal of Plasma Physics*, 38, 169.
doi:10.1017/S0022377800012496
- Cairns, I. H. 1995, *Geophys. Res. Lett.*, 22, 3433.
doi:10.1029/95GL03331
- Cairns, I. H. 1988, *J. Geophys. Res.*, 93, 858.
doi:10.1029/JA093iA02p00858
- Cairns, I. H. 1998, *ApJ*, 506, 456. doi:10.1086/306215
- Cairns, I. H. & Zank, G. P. 2002, *Geophys. Res. Lett.*, 29, 1143.
doi:10.1029/2001GL014112
- Che, H., Goldstein, M. L., Diamond, P. H., et al. 2017, *Proceedings of the National Academy of Science*, 114, 1502.
doi:10.1073/pnas.1614055114
- Chen, Y., Zhang, Z., Ni, S., et al. 2022, *ApJL*, 924, L34.
doi:10.3847/2041-8213/ac47fa
- Chen, Y., Du, G., Feng, L., et al. 2014, *ApJ*, 787, 59.
doi:10.1088/0004-637X/787/1/59
- Etcheto, J. & Faucheux, M. 1984, *J. Geophys. Res.*, 89, 6631.
doi:10.1029/JA089iA08p06631
- Ginzburg, V. L. & Zhelezniakov, V. V. 1958, *Soviet Ast.*, 2, 653
- Gurnett, D. A., Allendorf, S. C., & Kurth, W. S. 1998, *Geophys. Res. Lett.*, 25, 4433. doi:10.1029/1998GL900201

- Henri, P., Sgattoni, A., Briand, C., et al. 2019, *Journal of Geophysical Research (Space Physics)*, 124, 1475. doi:10.1029/2018JA025707
- Kasaba, Y., Matsumoto, H., & Omura, Y. 2001, *J. Geophys. Res.*, 106, 18693. doi:10.1029/2000JA000329
- Kliem, B., Krueger, A., & Treumann, R. A. 1992, *SoPh*, 140, 149. doi:10.1007/BF00148435
- Krafft, C. & Savoini, P. 2022, *ApJL*, 934, L28. doi:10.3847/2041-8213/ac7f28
- Kuncic, Z. & Cairns, I. H. 2005, *Journal of Geophysical Research (Space Physics)*, 110, A07107. doi:10.1029/2004JA010953
- Kundu, M. R. 1965, New York: Interscience Publication, 1965
- Lee, S.-Y., Ziebell, L. F., Yoon, P. H., et al. 2019, *ApJ*, 871, 74. doi:10.3847/1538-4357/aaf476
- Lee, S.-Y., Yoon, P. H., Lee, E., et al. 2022, *ApJ*, 924, 36. doi:10.3847/1538-4357/ac32bb
- Li, C. Y., Chen, Y., Wang, B., et al. 2017, *SoPh*, 292, 82. doi:10.1007/s11207-017-1108-1
- Lin, R. P., Potter, D. W., Gurnett, D. A., et al. 1981, *ApJ*, 251, 364. doi:10.1086/159471
- Lin, R. P., Levedahl, W. K., Lotko, W., et al. 1986, *ApJ*, 308, 954. doi:10.1086/164563
- Lin, R. P., Evans, L. G., & Fainberg, J. 1973, *Astrophys. Lett.*, 14, 191
- Lv, M. S., Chen, Y., Li, C. Y., et al. 2017, *SoPh*, 292, 194. doi:10.1007/s11207-017-1218-9
- Matsumoto, H., & Omura, Y. 1993, in *Computer Space Plasma Physics: Simulation Techniques and Software*, ed. H. Matsumoto & Y. Omura (Tokyo: Terra Sci. Pub.)
- Melrose, D. B. 1980, *SSRv*, 26, 3. doi:10.1007/BF00212597
- Melrose, D. B. 1987, *SoPh*, 111, 89. doi:10.1007/BF00145443
- Melrose, D. B. 1970a, *Australian Journal of Physics*, 23, 871. doi:10.1071/PH700871
- Melrose, D. B. 1970b, *Australian Journal of Physics*, 23, 885. doi:10.1071/PH700885
- Ni, S., Chen, Y., Li, C., et al. 2020, *ApJL*, 891, L25. doi:10.3847/2041-8213/ab7750
- Pfša, D., Kurth, W. S., Hospodarsky, G. B., et al. 2017, *European Planetary Science Congress*
- Reid, H. A. S., Vilmer, N., & Kontar, E. P. 2014, *A&A*, 567, A85. doi:10.1051/0004-6361/201321973
- Reiner, M. J. & MacDowall, R. J. 2019, *SoPh*, 294, 91. doi:10.1007/s11207-019-1476-9
- Reiner, M. J., Stone, R. G., & Fainberg, J. 1992, *ApJ*, 394, 340. doi:10.1086/171586
- Rhee, T., Ryu, C.-M., Woo, M., et al. 2009, *ApJ*, 694, 618. doi:10.1088/0004-637X/694/1/618
- Robinson, P. A., Cairns, I. H., & Willes, A. J. 1994, *ApJ*, 422, 870. doi:10.1086/173779
- Pritchett, P. L. & Dawson, J. M. 1983, *Physics of Fluids*, 26, 1114. doi:10.1063/1.864222
- Takakura, T. & Yousef, S. 1974, *SoPh*, 36, 451. doi:10.1007/BF00151214
- Tasnim, S., Zank, G. P., Cairns, I. H., et al. 2022, *ApJ*, 928, 125. doi:10.3847/1538-4357/ac5031
- Thurgood, J. O. & Tsiklauri, D. 2015, *A&A*, 584, A83. doi:10.1051/0004-6361/201527079
- Vasanth, V., Chen, Y., Lv, M., et al. 2019, *ApJ*, 870, 30. doi:10.3847/1538-4357/aaeffd
- Vasanth, V., Chen, Y., Feng, S., et al. 2016, *ApJL*, 830, L2. doi:10.3847/2041-8205/830/1/L2
- Wild, J. P. & McCreedy, L. L. 1950, *Australian Journal of Scientific Research A Physical Sciences*, 3, 387. doi:10.1071/CH9500387
- Wild, J. P., Sheridan, K. V., & Neylan, A. A. 1959, *Australian Journal of Physics*, 12, 369. doi:10.1071/PH590369
- Yi, S., Yoon, P. H., & Ryu, C.-M. 2007, *Physics of Plasmas*, 14, 013301. doi:10.1063/1.2424556
- Yin, L., Ashour-Abdalla, M., El-Alaoui, M., et al. 1998, *Geophys. Res. Lett.*, 25, 2609. doi:10.1029/98GL01989
- Yoon, P. H., Ziebell, L. F., Gaelzer, R., et al. 2012, *Physics of Plasmas*, 19, 102303. doi:10.1063/1.4757224
- Yoon, P. H. 2006, *Physics of Plasmas*, 13, 022302. doi:10.1063/1.2167587
- Yoon, P. H. 2000, *Physics of Plasmas*, 7, 4858. doi:10.1063/1.1318358
- Yoon, P. H. 2005, *Physics of Plasmas*, 12, 042306. doi:10.1063/1.1864073
- Zhang, Z., Chen, Y., Ni, S., et al. 2022, *ApJ*, 939, 63. doi:10.3847/1538-4357/ac94c6
- Zheleznyakov, V. V. & Zlotnik, E. Y. 1974, *SoPh*, 36, 443. doi:10.1007/BF00151213
- Zheleznyakov, V. V. & Zaitsev, V. V. 1970a, *Soviet Ast.*, 14, 250
- Zheleznyakov, V. V. & Zaitsev, V. V. 1970b, *Soviet Ast.*, 14, 47
- Ziebell, L. F., Petruzzellis, L. T., Yoon, P. H., et al. 2016, *ApJ*, 818, 61. doi:10.3847/0004-637X/818/1/61
- Ziebell, L. F., Yoon, P. H., Petruzzellis, L. T., et al. 2015, *ApJ*, 806, 237. doi:10.1088/0004-637X/806/2/237
- Zlotnik, E. I. 1978, *Soviet Ast.*, 22, 228
- Zlotnik, E. Y., Klassen, A., Klein, K.-L., et al. 1998, *A&A*, 331, 1087

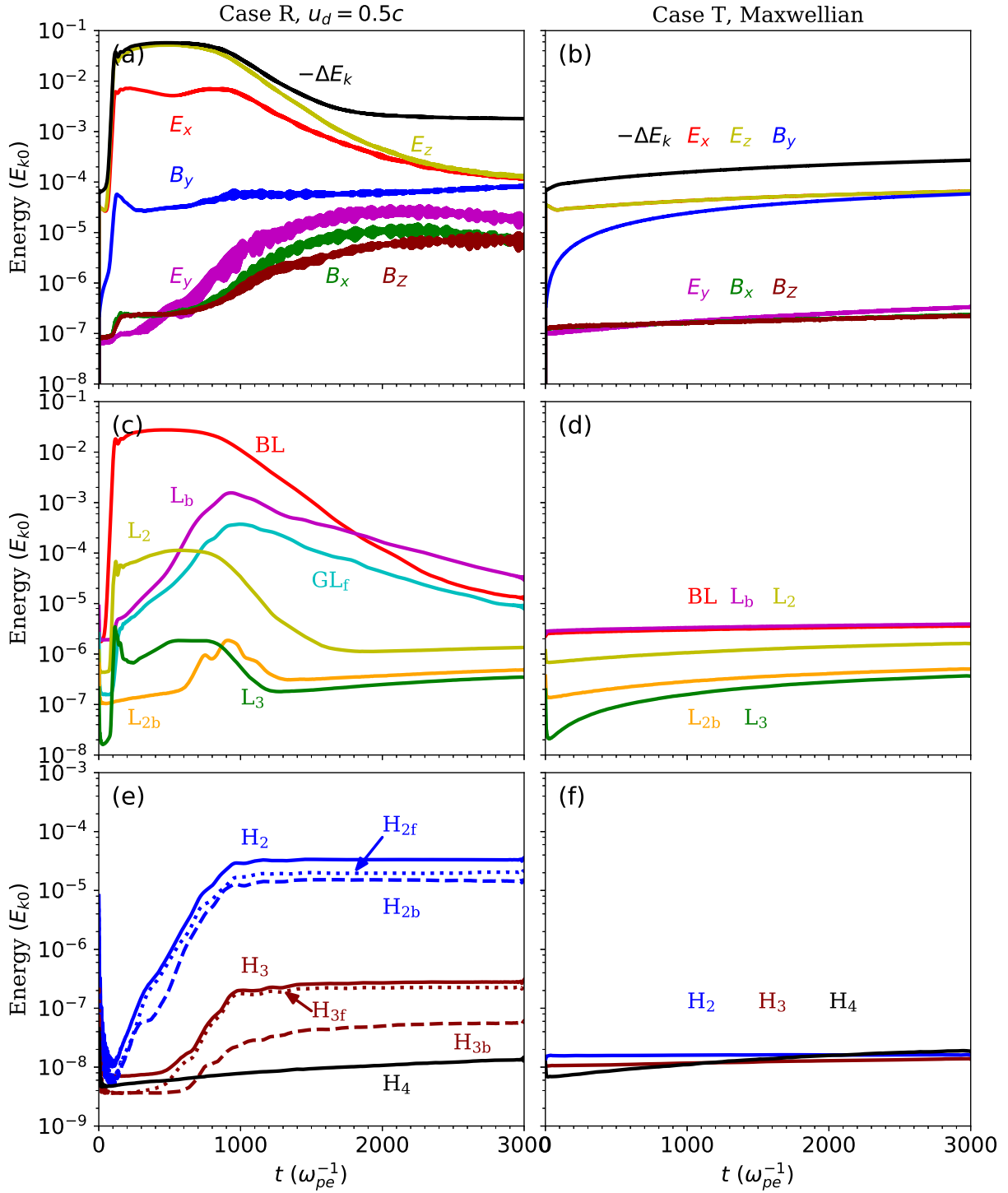


Figure 1. (a) and (b) Temporal profiles of energies of various field components (E_x , E_y , E_z , B_x , B_y , and B_z) and the negative change of the total electron energy ($-\Delta E_k$). Temporal energy profiles of different modes, where (c) and (d) are for the ES modes and (e) and (f) are for the EM radiation. The subscripts “f” and “b” indicate the forward- and backward-propagating parts of the respective modes, while the subscript numbers represent the corresponding harmonics. The left column presents the results of Case R, and the right column displays the corresponding thermal Case T. The values in the plots are normalized by the respective initial kinetic energy of total electrons (E_{k0}).

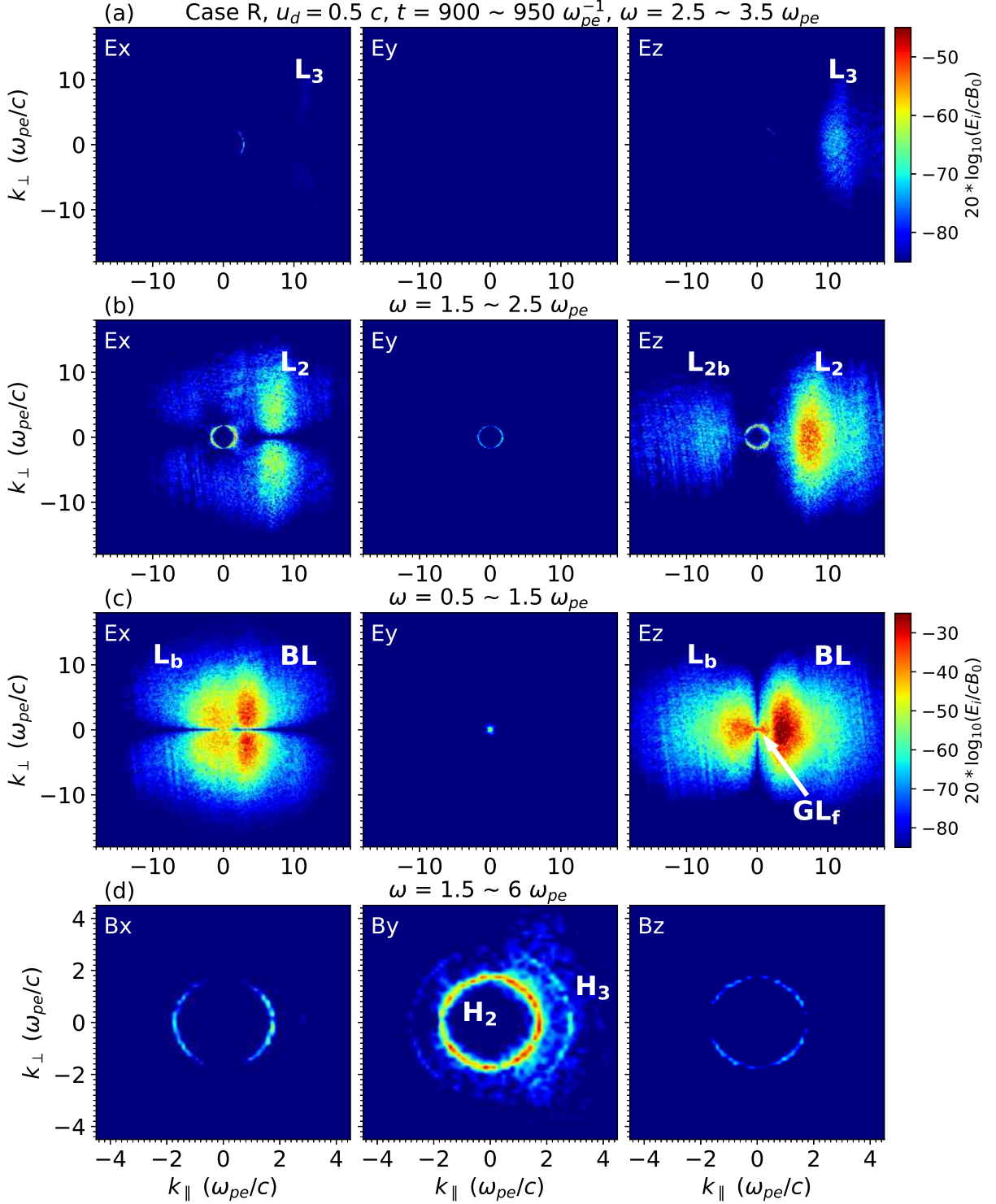


Figure 2. Maximum intensity of the six field components in the ω domain ((a) 2.5–3.5, (b) 1.5–2.5, (c) 0.5–1.5, and (d) 1.5–6 ω_{pe}) as a function of k_{\parallel} and k_{\perp} over the interval of $900 < \omega_{pe}t < 950$ for Case R. The upper three rows illustrate the corresponding ES modes, while the fourth row represents the EM radiation displayed by the magnetic field components. An animation of this figure is available. The animation begins with the map for the interval of $[0, 50] \omega_{pe}^{-1}$ and ends with that for the interval of $[2950, 3000] \omega_{pe}^{-1}$. The real-time duration of the video is 12 s.

(An animation of this figure is available.)

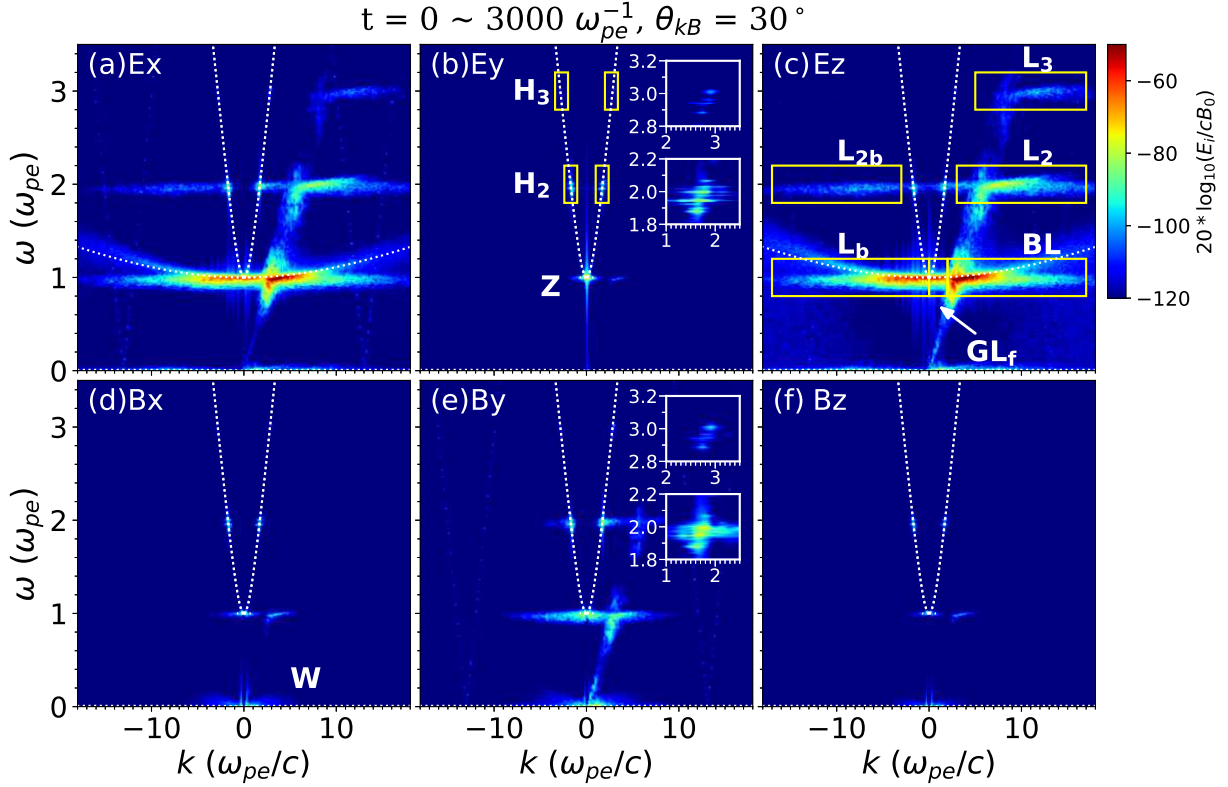


Figure 3. Wave dispersion diagrams of the six field components along $\theta_{kB} = 0^\circ$ (θ_{kB} is the angle between the wavevector, \vec{k} , and the background magnetic field, \vec{B}_0). The curve near ω_{pe} in panel (c) represents the dispersion relation of L wave with thermal effects ($\omega^2 = \omega_{pe}^2(1 + 3k^2\lambda_{De}^2)$), while the other white dashed lines represent the dispersion curves given by the magnetoionic theory. “Z” denotes the Z mode, and “W” denotes the whistler mode. The yellow boxes mark the regions selected for the evaluation of mode energy. The white boxes in panels (b) and (e) zoom in on the H_2 and H_3 spectra. An animation of this figure is available. The animation begins at $\theta_{kB} = 0^\circ$ and advances 10° at a time up to $\theta_{kB} = 90^\circ$. The real-time duration of the video is 3 s.

(An animation of this figure is available.)

Table 1. Ranges of ω and k for each mode at the moment before the rapid decay of each ES harmonic mode ($\sim 900 \omega_{pe}^{-1}$) for Case R.

	BL	L _b	GL _f	L ₂	L _{2b}	L ₃	H ₂	H ₃
$\omega (\omega_{pe})$	0.8–1.18	0.88–1.04	0.9–1	1.8–2.06	1.88–2	2.9–3.06	1.88–2.06	2.89–3.01
$k (\omega_{pe}/c)$	2–15	-15–0	0–2	5–15	-10~4	9–13	-1.8–1.8	-2.8–2.8

Table 2. The intensity ratios of H_2/H_3 and H_3/H_4 at saturation for Cases R and A–E. The energy ratios of the forward- (f) and backward- (b) propagating portions for H_2 , H_3 , and H_4 are also listed.

	Case A	Case B	Case R	Case C	Case D	Case E
W_{H2}/W_{H3}	206.8	169.3	120.0	58.3	44.1	124.8
W_{H3}/W_{H4}	–	–	–	93.6	88.5	–
W_{H2f}/W_{H2b}	2.8	3.0	1.4	1.6	0.8	4.3
W_{H3f}/W_{H3b}	0.3	0.7	4.0	7.5	8.5	1.1
W_{H4f}/W_{H4b}	–	–	–	1.4	3.7	–

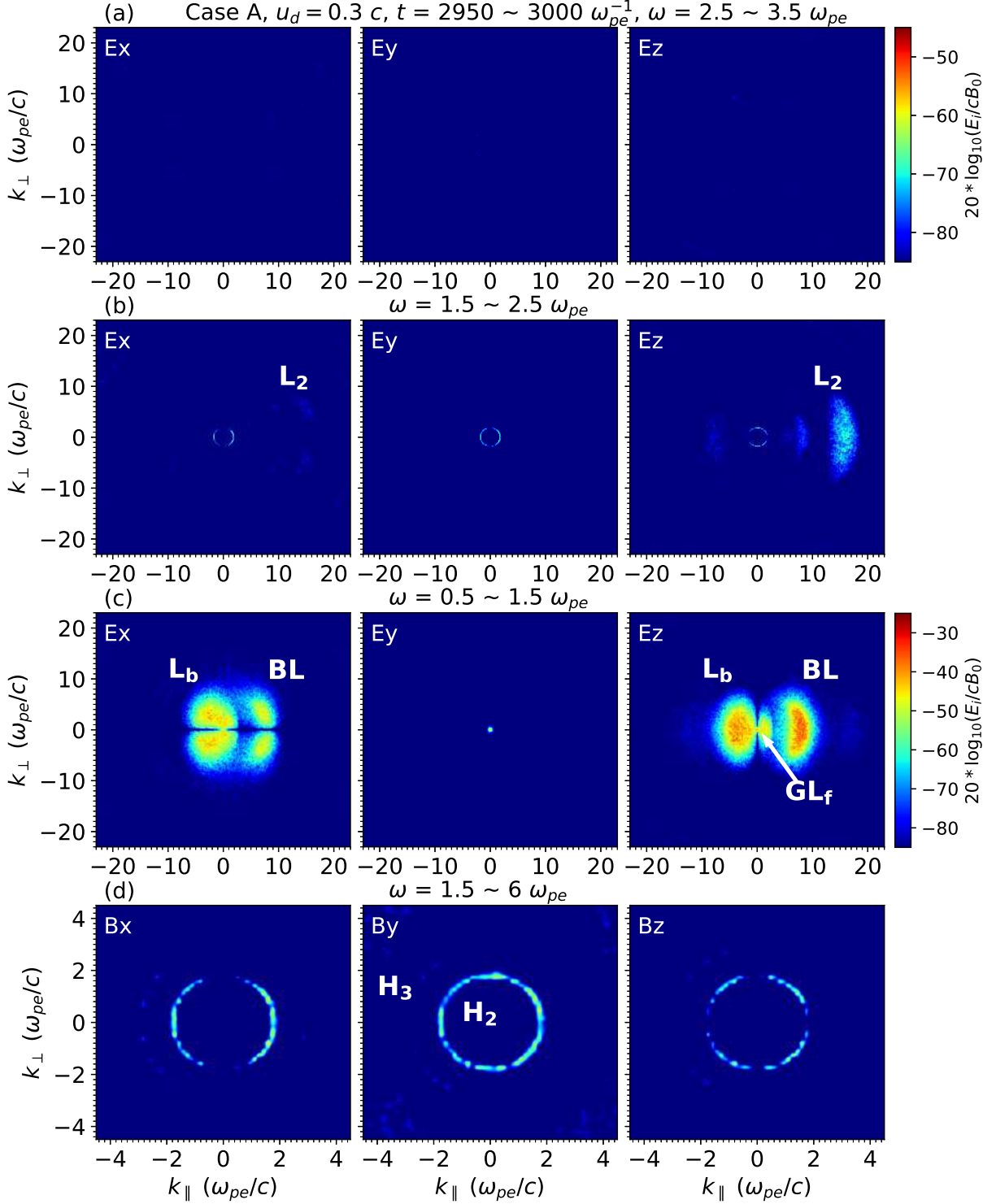


Figure 4. Maximum intensity of the six field components in the ω domain ((a) 2.5–3.5, (b) 1.5–2.5, (c) 0.5–1.5, and (d) 1.5–6 ω_{pe}) as a function of k_{\parallel} and k_{\perp} over the interval of $2950 < \omega_{pe}t < 3000$ for Case A. The upper three rows illustrate the corresponding ES modes, while the fourth row represents the EM radiation displayed by the magnetic field components. An animation of this figure is available, and it presents the mode evolution for Cases A, B and E, with each part beginning with the map for the interval of $[0, 50] \omega_{pe}^{-1}$ and ending with that for the interval of $[2950, 3000] \omega_{pe}^{-1}$. The real-time duration of the video is 36 s.

(An animation of this figure is available.)

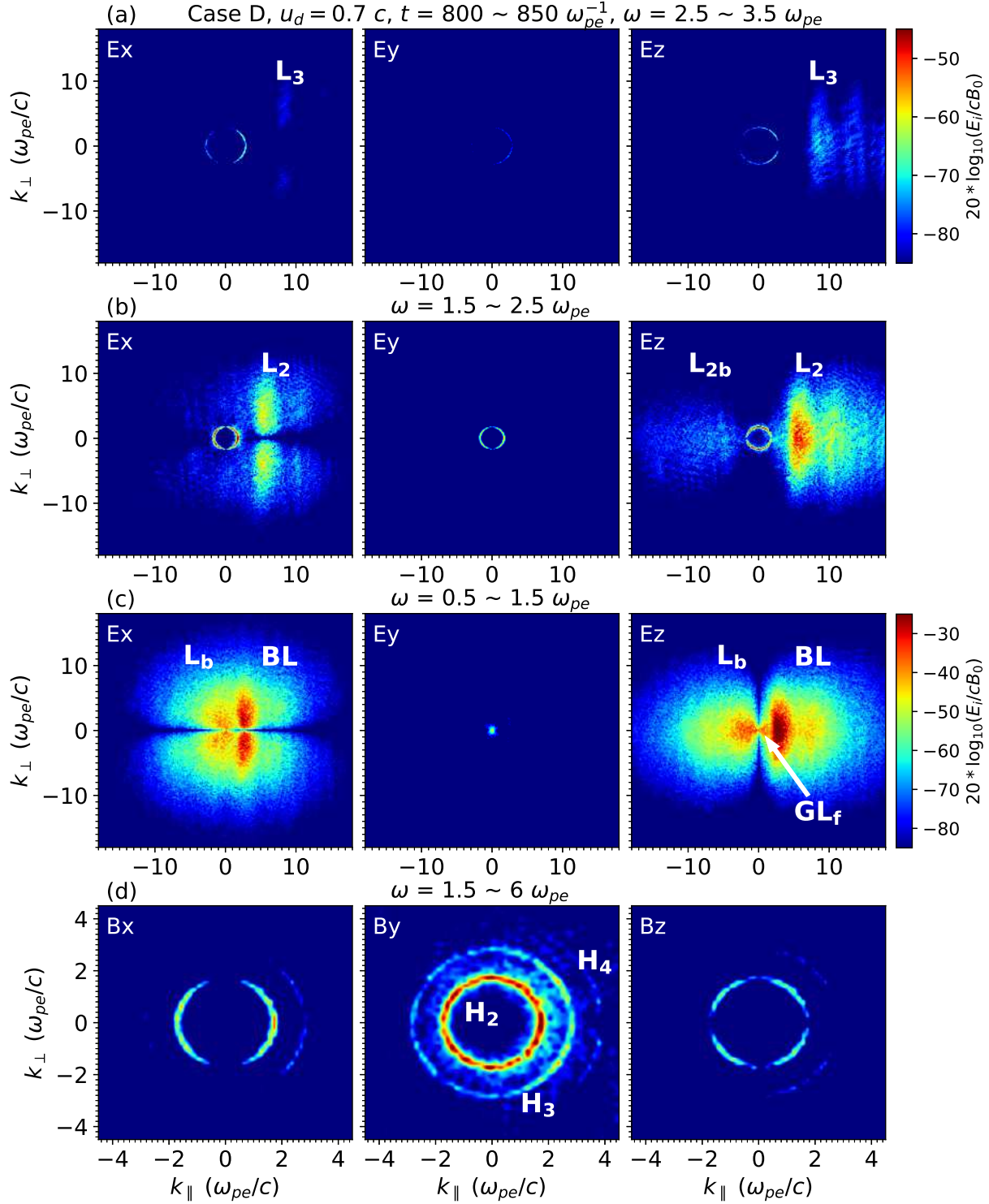


Figure 5. Maximum intensity of the six field components in the ω domain ((a) 2.5–3.5, (b) 1.5–2.5, (c) 0.5–1.5, and (d) 1.5–6 ω_{pe}) as a function of k_{\parallel} and k_{\perp} over the interval of $800 < \omega_{pe}t < 850$ for Case D. The upper three rows illustrate the corresponding ES modes, while the fourth row represents the EM radiation displayed by the magnetic field components. The video begins with the map for the interval of $[0, 50] \omega_{pe}^{-1}$, ending with that for the interval of $[2950, 3000] \omega_{pe}^{-1}$. The real-time duration of the video is 12 s.

(An animation of this figure is available.)

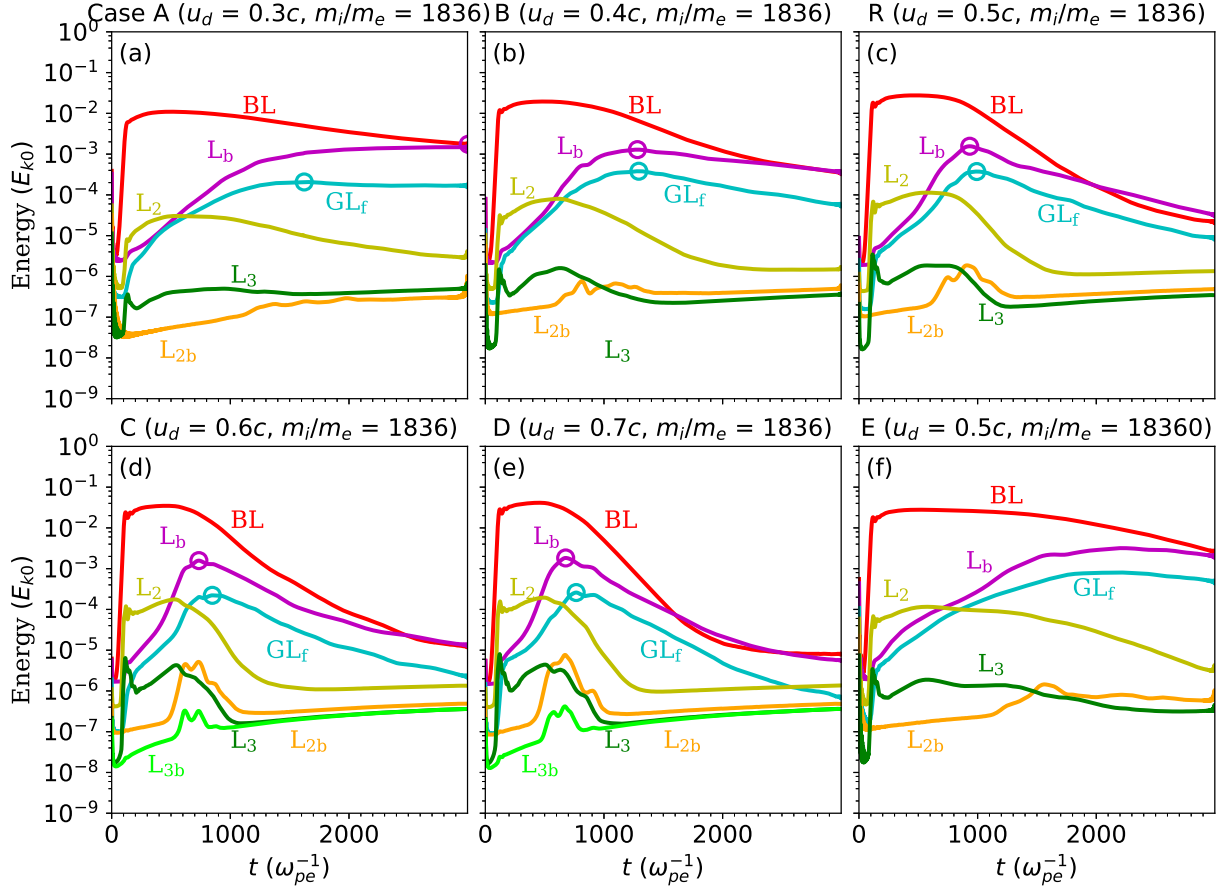


Figure 6. The temporal energy profiles of the ES harmonic modes (BL, L_b , GL_f , L_2 , L_{2b} , L_3 , L_{3b}), normalized by the respective initial kinetic energy of total electrons (E_{k_0}). (a)–(e) are for cases with $m_i/m_e = 1836$ and $u_d = 0.3$ – $0.7c$, and (f) is for Case E with $u_d = 0.5c$ and $m_i/m_e = 18360$. The magenta and cyan circles in panels (a)–(e) mark the intensity maxima of the L_b and GL_f modes, respectively.

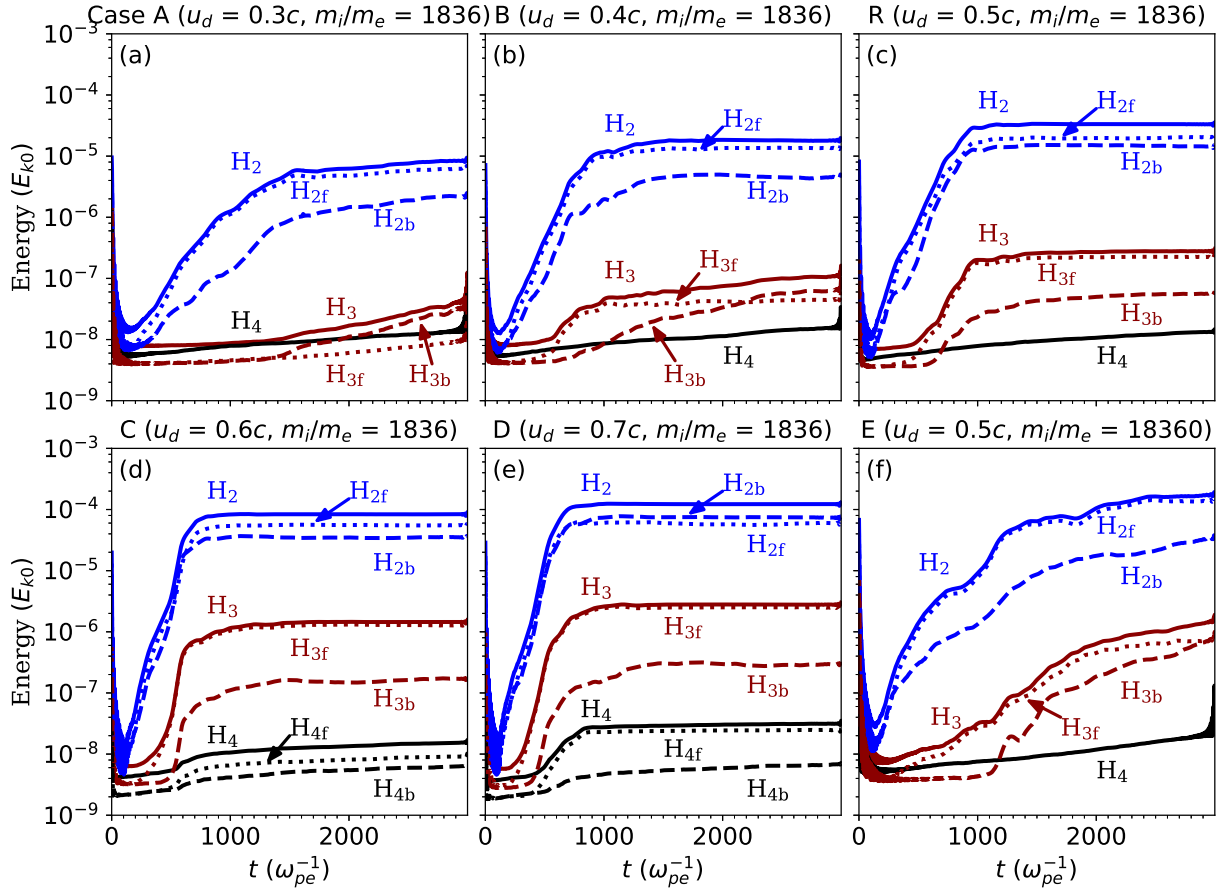


Figure 7. The temporal energy profiles of the second, third, and fourth EM harmonic emission. The solid lines represent the sum of the energy in each direction of the corresponding harmonic emission, and the dotted and dashed lines represent the forward (f; $k_{\parallel} > 0$) and backward (b; $k_{\parallel} < 0$) propagation part of the energy of the corresponding radiation, respectively. The values in the figures are normalized by the respective initial kinetic energy of total electrons (E_{k_0}).